# Long-duration gamma-ray emissions from 2007 and 2008 winter thunderstorms

H. Tsuchiya,[1] T. Enoto,[2] S. Yamada,[3] T. Yuasa,[3] K. Nakazawa,[3] T.

Kitaguchi,[4] M. Kawaharada,[5] M. Kokubun,[5] H. Kato,[1] M. Okano,[1] and K.

Makishima[3]

3  **Abstract.**     The Gamma-Ray Observation of Winter THunderclouds (GROWTH)

4  experiment, consisting of two radiation-detection subsystems, has been op-

---

H. Tsuchiya, High-energy Astrophysics Laboratory, Riken, 2-1, Hirosawa, Wako, Saitama 351-0198, Japan. (htsuchiya@riken.jp)

T. Enoto, Kavli Institute for Particle Astrophysics and Cosmology, Department of Physics and SLAC National Accelerator Laboratory, Stanford University, Stanford, CA 94305, USA (enoto@stanford.edu)

S. Yamada, Department of Physics, University of Tokyo, 7-3-1, Hongo, Bunkyo-ku, Tokyo 113-0033, Japan. (yamada@juno.phys.s.u-tokyo.ac.jp)

T. Yuasa, Department of Physics, University of Tokyo, 7-3-1, Hongo, Bunkyo-ku, Tokyo 113-0033, Japan. (yuasa@juno.phys.s.u-tokyo.ac.jp)

K. Nakazawa, Department of Physics, University of Tokyo, 7-3-1, Hongo, Bunkyo-ku, Tokyo 113-0033, Japan. (nakazawa@phys.s.u-tokyo.ac.jp)

T. Kitaguchi, Division of Physics, Mathematics, and Astronomy, California Institute of Technology, 1200 East California Boulevard, Pasadena, CA 91125, USA (kitaguti@caltech.edu)

M. Kawaharada, Department of High Energy Astrophysics, Institute of Space and Astronautical Science, JAXA, 3-1-1, Chuo-ku, Sagamihara, Kanagawa 252-5210, Japan. (kawahard@astro.isas.jaxa.jp)

M. Kokubun, Department of High Energy Astrophysics, Institute of Space and Astronautical Science, JAXA, 3-1-1, Chuo-ku, Sagamihara, Kanagawa 252-5210, Japan. (kokubun@astro.isas.jaxa.jp)

H. Kato, High-energy Astrophysics Laboratory, Riken, 2-1, Hirosawa, Wako, Saitama 351-0198,

erating since 2006 on the premises of Kashiwazaki-Kariwa nuclear power plant

located at the coastal area of Japan Sea. By 2010 February, GROWTH de-

tected 7 long-duration $\gamma$-rays emissions associated with winter thunderstorms.

Of them, two events, obtained on 2007 December 13 and 2008 December 25,

are reported. On both occasions, all inorganic scintillators (NaI, CsI, and BGO)

of the two subsystems detected significant $\gamma$-ray signals lasting for >1 minute.

Neither of these two events were associated with any lightning. In both cases,

the $\gamma$-ray energy spectra extend to 10 MeV, suggesting that the detected $\gamma$-

rays are produced by relativistic electrons via bremsstrahlung. Assuming that

the initial photon spectrum at the source is expressed by a power-law func-

tion, the observed photons can be interpreted as being radiated from a source

located at a distance of $290 - 560$ m for the 2007 event and $110 - 690$ m

for the 2008 one, both at 90% confidence level. Employing these photon spec-

tra, the number of relativistic electrons is estimated as $10^9 - 10^{11}$. The es-

timation generally agrees with those calculated based on the relativistic run-

away electron avalanche model. A GROWTH photon spectrum, summed over

3 individual events including the present two events and another reported

Japan. (hkato@riken.jp)

M. Okano, High-energy Astrophysics Laboratory, Riken, 2-1, Hirosawa, Wako, Saitama 351-0198, Japan. (mokano@crab.riken.jp)

K. Makishima, Department of Physics, University of Tokyo, 7-3-1, Hongo, Bunkyo-ku, Tokyo 113-0033, Japan. (maxima@phys.s.u-tokyo.ac.jp)

previously, has similar features including a cut-off energy, to an averaged spec-

trum of terrestrial gamma-ray flashes.

## 1. Introduction

Nonthermal X-ray and $\gamma$ ray emission, typically lasting for a few seconds to $\sim 10$ minutes, has been observed from thunderstorm activity, with detectors on board an airplane [*McCarthy and Parks*, 1985] and a ballon [*Eack et al.*, 1996, 2000], high-mountain detectors [*Suszcynsky et al.*, 1996; *Brunetti et al.*, 2000; *Chubenko et al.*, 2000; *Alexeenko et al.*, 2002; *Muraki et al.*, 2004; *Torii et al.*, 2009; *Tsuchiya et al.*, 2009; *Chilingarian et al.*, 2010], and ground-based ones [*Torii et al.*, 2002; *Tsuchiya et al.*, 2007]. Interestingly, they do not appear to clearly coincide with lightning processes such as stepped leaders or return strokes. In contrast, much shorter energetic radiation bursts, lasting only for tens of milliseconds or less, are often associated with lightning discharges. Though not necessarily homogeneous, they include terrestrial gamma-ray flashes (TGFs) [*Fishman et al.*, 1994; *Smith et al.*, 2005; *Grefenstette et al.*, 2009; *Briggs et al.*, 2010; *Connaughton et al.*, 2010; *Marisaldi et al.*, 2010a, b], natural lightning [*Moore et al.*, 2001; *Dwyer et al.*, 2005; *Howard et al.*, 2008; *Yoshida et al.*, 2008; *Chubenko et al.*, 2009], and rocket-trigerred ones [*Dwyer et al.*, 2003, 2004a, b].

In this way, it has recently become clear that apparently two types of radiation bursts with distinct duration are associated with thunderstorm activity. Although it is uncertain whether or not these two types have a common source mechanism, recent observations as well as theoretical works generally suggest that these bursts, especially short-duration ones, are produced by processes involving acceleration and multiplication of a background population of electrons.

Various numerical kinetic calculations [*Gurevich et al.*, 1992; *Roussel-Dupré et al.*, 1994; *Bell et al.*, 1995; *Lehtinen et al.*, 1996; *Gurebich et al.*, 1997; *Milikh and Valdia*, 1999; *Gurevich et al.*, 2007; *Roussel-Dupré et al.*, 2008] and Monte Carlo simulations [*Lehtinen et al.*, 1999; *Dwyer*, 2003; *Babich et al.*, 2005, 2007] commonly indicate that most of prompt nonthermal photons from lightning discharges are radiated, via bremsstrahlung, by relativistic electrons, which in turn are produced through mechanism involving relativistic runaway electron avalanche (RREA): some seed electrons, produced by e.g. cosmic rays, can be accelerated into relativistic regime if they can gain energies from the high electric fields in thunderclouds fast enough to overcome their total energy losses, due mainly to ionization. Then, they collide with air molecules and ionize them. Some of the faster newborn secondary electrons are also accelerated to higher energies, hence increasing in their number. Finally, they will emit a detectable flux of nonthermal photons via bremsstrahlung.

Early observations of long-duration bursts, though limited in number, measured X-ray fluxes in a few keV to a few hundred keV range, or $\gamma$-ray fluxes in MeV regions, suggesting that these prolonged emissions are also due to relativistic electrons [*McCarthy and Parks*, 1985; *Eack et al.*, 1996, 2000; *Brunetti et al.*, 2000; *Chubenko et al.*, 2000]. Several recent observations [*Tsuchiya et al.*, 2007; *Torii et al.*, 2009; *Tsuchiya et al.*, 2009; *Chilingarian et al.*, 2010] have reinforced the suggestion, by detecting photon spectra extending clearly to 10 MeV or higher, and have given evidence that those long-duration $\gamma$ rays are also produced via bremsstrahlung. These results naturally lead to a view that long-duration events are also caused by relativistic runaway electrons. However, compared with short-duration ones, the nature of long-duration bursts have remained less understood, due primary to the lack of a sufficiently large sample. For example, it is still unclear how the

67 electron acceleration process keeps operating for such long durations. In addition, the

68 relation between short-duration bursts and long-duration ones is unknown.

69 Aiming at detections of radiation bursts from thunderstorm activity, we have been op-

70 erating the Gamma-Ray Observations of Winter THunderclouds (GROWTH) experiment

71 since 2006 December 20. In this paper, we report on successful GROWTH detections

72 of two long-duration $\gamma$-ray bursts extending to 10 MeV. Using the acquired $\gamma$-ray data,

73 the source distance, its spatial extent, and the number of relativistic electrons involved

74 therein are estimated. Then, a $\gamma$-ray spectrum which sums up 3 GROWTH detections is

75 compared with cumulative TGF spectra obtained by two independent space observations.

76 Based on these results, we quantitatively discuss the production mechanism of prolonged

77 $\gamma$-ray bursts from winter thunderclouds.

## 2. The GROWTH Experiment

78 The GROWTH experiment, comprising two independent subsystems, has been oper-

79 ating successfully at a roof of a building of Kashiwazaki-Kariwa nuclear power plant in

80 Niigata Prefecture, Japan. Figure 1 shows the location of the plant, facing the Japan Sea,

81 and the GROWTH experimental site therein. The geographical longitude, latitude, and

82 altitude of the experimental site are $138°36'$E, $37°26'$N, and 40 m above sea level, respec-

83 tively. This coastal area is frequently struck by strong thunderstorms in winter seasons.

84 Actually, before the GROWTH experiment started working, radiation monitors (filled

85 circles in Fig. 1), which are arranged at around 300 m − 400 m intervals in the plant,

86 occasionally observed > 3 MeV intense radiation enhancements in winter seasons, which

87 are difficult to ascribe to so-called radon washouts because these rainfall-related episodes

88 would mainly cause increases at < 3 MeV energies [e.g. *Yoshioka*, 1992; *Yamazaki et al.*,

2002]. Each radiation monitor consists of a $\phi 5.1\,\mathrm{cm} \times 5.1\,\mathrm{cm}$ NaI (Tl) scintillation counter,

and a spherical ion chamber with a volume of $\sim 14$ L that contains Ar gas. The former

covers the 50 keV $-$ 3 MeV energy range, while the later operates in $> 50$ keV. However,

the radiation monitors have too poor a time resolution of 30 sec, together with the too

limited energy bands, to understand the nature of those phenomena. The GROWTH

experiment is expected to provide much improved knowledge on these sporadic events.

The pictures and drawings of the two subsystems are given in *Enoto et al.* [2007] and

*Tsuchiya et al.* [2007]. One of them (Detector-A) uses two cylindrical NaI (Tl) scin-

tillators (density $= 3.67\,\mathrm{gcm}^{-3}$), having a diameter and a height of both 7.62 cm. In

order to actively shield them from natural low-energy ($< 3$ MeV) environmental radiation

(e.g. from $^{40}$K), the NaI scintillators are individually surrounded by well-shaped BGO

($\mathrm{Bi_4Ge_3O_{12}}$; density $= 7.1\,\mathrm{gcm}^{-3}$) scintillators, with the thickness on the side and bottom

being 1.27 cm and 2.54 cm, respectively. The BGO scintillators geometrically shield the

central NaI up to a solid angle of $2.4\pi$ str, or $0.6 \times 4\pi$. Thus, the NaI scintillators have

a higher sensitivity toward the sky direction. The two central NaI scintillators and the

BGO shields are operated over an energy range of 40 keV $-$ 10 MeV. Output signals from

photomultiplier tubes, attached to the NaI and BGO, are fed individually to a 12 bit 8ch

VME-analog-to-digital converter [ADC (CP 1113A)] with a time resolution of 10 $\mu$sec,

and is recorded on event-by-event basis.

As another feature of Detector-A, a 0.5 cm thick plastic scintillator with an area of

$30.5\,\mathrm{cm} \times 15.2\,\mathrm{cm} = 464\,\mathrm{cm}^2$ is placed above the two NaI scintillators, and operated with

a threshold energy of $> 1$ MeV. It has a high detection efficiency for charged particles,

while it is almost transparent to photons due to its thinness and higher threshold. Utiliz-

112  ing this feature, we can separate charged particles from photons, and efficiently exclude

113  background cosmic-ray muons, which typically deposit $> 1$ MeV energies, from events in

114  the two NaI scintillators. Specifically, an event in either of the two NaI scintillators is

115  judged as a charged particle if it give a simultaneous hit (with 10 $\mu$ sec) in the plastic

116  scintillator. Thus, utilizing signals of the BGO and plastic scintillators both in anticoin-

117  cidence, the central NaI scintillators effectively detect photons, generally arriving from a

118  sky direction.

119      Aiming at an independent radiation measurement, another subsystem (Detector-B) was

120  installed $\sim 10$ m apart from Detector-A. It consists of spherical NaI (Tl) and CsI (Tl)

121  scintillators (density $= 4.51\,\mathrm{g cm}^{-3}$), both with a diameter of 7.62 cm. The former op-

122  erates in 40 keV $-10$ MeV, while the latter covers a higher energy range of 300 keV $-$

123  80 MeV. Unlike Detector-A, these scintillators have omni-directional sensitivity because

124  they have no shields such as the BGO or plastic scintillators. Output signals of two pho-

125  tomultiplier tubes, attached to the NaI and CsI crystals, are sampled by a self-triggering

126  electronics system with a 12 bit ADC (AD 574). These events are accumulated into an

127  ADC histogram, which is recorded every 6 sec.

128      Energy calibrations of Detector-A and Detector-B were carried out, using natural envi-

129  ronmental $\gamma$-ray lines of $^{214}$Pb (0.352 MeV), $^{214}$Bi (0.609 MeV), $^{40}$K (1.46 MeV), and $^{208}$Tl

130  (2.61 MeV). Then, especially for the CsI of Detector-B, cosmic-ray muons, giving energy

131  deposits with its peak of around 35 MeV, were also utilized. Basically, these calibrations

132  are performed and checked by an offline analysis.

133      In addition to those radiation detectors, the GROWTH system utilizes three optical

134  sensors and an electric-field mill as environmental monitors. Each optical sensor consists

135  of a hand-made analog circuit, and a silicon photodiode (HAMAMATSU S1226-8BK)

136  which is sensitive over a wavelength range of 320 nm − 1000 nm (with its peak at 750

137  nm). They measure environmental visible light in coarsely different directions; sea side,

138  zenith direction, and anti-sea side. The output signals are fed to a 12 bit VME-ADC, and

139  recorded every 0.1 sec. The electric field mill is a commercial product (BOLTEK EFM-

140  100). Its analog output is fed to a 12 bit ADC (AD 7892), and recored as electric-field

141  strength between $\pm 100\,\mathrm{kV}\,\mathrm{m}^{-1}$, with a resolution of 50 $\mathrm{Vm}^{-1}$.

## 3. Results

### 3.1. Count histories of the inorganic scintillators

142  Figure 2 shows count histories of the 4 inorganic scintillators of Detector-A and B,

143  obtained over 15:00 − 17:00 UT on 2007 December 13 which corresponds to local midnight

144  (0:00 − 2:00 JST on 2007 December 14). For reference, typical background rates per 20

145  sec, corresponding to the panels (a), (b), (c), and (d) of Fig. 2, are 22000, 1700, 2100, and

146  1500, respectively. Similarly, Figure 3 gives those over 8:30 − 10:30 UT on 2008 December

147  25 (17:30 − 19:30 JST on the same day, or local evening). On both these days, a strong

148  low pressure system (with ∼ 990 hPa on the ground) developed over Japan, causing

149  thunderstorms at the coastal area of Japan Sea. A gradual count increase, followed by a

150  gradual count decrease, generally shows that they are due mainly to radioactive radon and

151  its decay products in rain,with their half-lives being 20 − 30 min. These effects originating

152  from radionuclides are closely investigated by *Suszcynsky et al.* [1996] and *Yamazaki et al.*

153  [2002].

154  Superimposed on such gradual count increases, a sharp count enhancement is found in all

155  the inorganic scintillators at around 16:00 UT in Fig. 2, and at around 9:30 UT in Fig. 3.

156   Hereafter, we call the former and the latter events 071213 and 081225, respectively. These

157   enhancements, both lasting for $70 - 80$ sec, are quite different from the radon effects and

158   from short radiation bursts associated with lightning discharges. Among those inorganic

159   scintillators, BGO of Detector-A gave statistically the most significant burst detection on

160   both occasions; $30\sigma$ for 071213 and $19\sigma$ for 081225. This is because it has a higher density

161   and a larger effective atomic number, and hence a higher stopping power, especially for

162   $X/\gamma$ rays, than the other inorganic scintillators used in our system.

163   Figure 4 shows NaI count histories of 071213 in 3 energy bands from Detector-A and

164   B, while Figure 5 represents those of 081225. For comparison with Detector-B, the data

165   of Detector-A [panels (a), (b) and (c) of Fig. 4 and Fig. 5] are presented without the

166   BGO or plastic anticoincidence. With a criterion that both the NaI and CsI scintillators

167   of Detector-B simultaneously record 10 or higher counts per 12 sec in the $3 - 10$ MeV

168   energy band, we define burst periods of 071213 and 081225 as 84 sec, $15:59:29 - 16:00:53$

169   UT, and 72 sec, $9:28:29 - 9:29:37$ UT, respectively. For reference, this energy band of

170   either scintillator typically records $\sim 4 - 5$ events per 12 sec in quiescent periods; so the

171   above criterion (again, not either but both scintillators have 10 or higher counts) means

172   approximately $\geq 3.2 - 4.0\sigma$ above the background.

173   In order to estimate background levels of individual energy bands of Detector-A and B,

174   we excluded data over the burst period (as defined above) and the adjacent 12-sec periods.

175   The remaining data in the two lower-energy bands were fitted by a quadratic function

176   (via $\chi^2$ evaluation), while those in the highest-energy band with a constant. Table 1

177   summarizes the net count increases, obtained by subtracting interpolated background

178   (dashed curves of Fig. 4 and Fig. 5) from the total counts in the burst period. Thus,

179 the burst detection is statistically significant in each of the three energy bands on both

180 occasions. Table 1 also gives the observed photon number fluxes above the detectors

181 using power-law spectra obtained later (Sec.3.5) and the detector responses of Detector

182 B derived from a Monte Carlo simulation based on GEANT4 [*Agostinelli et al.*, 2003].

183 Here, the MC simulation was evaluated with radionuclide sources of $^{60}$Co and $^{137}$Cs.

### 3.2. Arrival directions

184 Shown in Fig. 4 and Fig. 5 are the NaI count rates of Detector A at $> 3$ MeV energies

185 of 071213 and 081225, respectively, with [panel (d) in both figures] and without [panel

186 (c)] anticoincidence. In both figures, the anticoincidence, which utilizes BGO and plastic

187 signals in logical "OR", is seen to reduce the NaI background level (solid curves) to

188 $\sim 0.05$ times that without anticoincidence. In contrast, the NaI-detected burst signal rate

189 decreases due to the anticoincidence only to $0.25 \pm 0.03$ and $0.31 \pm 0.06$ times the raw rates,

190 for 071213 and 081225, respectively. Thus, the burst photons survive the anti-coincidence

191 with $5 - 6$ times higher efficiency than the background events. Similarly, the ratio of the

192 $> 40$ keV NaI [Fig. 2 (b) and Fig. 3 (b)] to the $> 40$ keV BGO count rates [Fig. 2 (a) and

193 Fig. 3 (a)], which is normally $\sim 0.08$ due mostly to environmental radioactivity coming

194 from omni-directions, increased to $0.18 \pm 0.02$ for 071213 and $0.14 \pm 0.02$ for 081225.

195 The above properties revealed by applying the anticoincidence are thought to reflect

196 arrival directions of the burst signals. If they came mainly from horizontal or ground

197 directions, the anticoincidence on/off ratio and the NaI/BGO ratio would both fall below

198 their normal values, because, e.g., 40 keV or 3 MeV $\gamma$ rays horizontally entering Detector-

199 A would be almost fully or partially (at least 30%) absorbed/scattered by BGO via

200 photoelectric absorption and Compton scattering. Accordingly, we conclude that the

201 burst signals arrived from sky directions, not from horizontal or ground directions. A

202 more quantitative study of arrival directions, employing Monte Carlo simulations, will be

203 reported elsewhere.

### 3.3. Burst components

204 Figure 6 shows count histories of the plastic scintillator ($> 1$ MeV) and the envi-

205 ronmental sensors. In coincidence with the apparent signals detected by the inorganic

206 scintillators, the 0.5 cm thick plastic scintillator gave count increases in individual burst

207 periods by $N_{pl} = 160 \pm 30\,(5.3\sigma)$ for 071213 and $72 \pm 18\,(4\sigma)$ for 081225 [top panels of

208 Fig. 6]. Presumably these plastic signals are composed of $\gamma$ rays and charged particles,

209 most likely electrons, which are either accelerated primaries or secondary ones produced

210 by high-energy photons via Compton scattering. Below, we estimate how $\gamma$ rays and

211 electrons contribute to $N_{pl}$, and estimate the electron flux above 1 MeV.

212 First, a Monte Carlo simulation using GEANT4 predicts that the plastic scintillator has

213 a low detection efficiency, $0.5 - 1\%$, for $> 1$ MeV $\gamma$ rays, while that for $> 1$ MeV electrons

214 reaches $75 - 90\%$. Next, using power-law spectra obtained later (Sec.3.5) and the effective

215 area of the NaI scintillator of Detector B yield $1 - 10$ MeV photon number fluxes above the

216 GROWTH system as $(17.9 \pm 1.8) \times 10^{-2}$ cm$^{-2}$s$^{-1}$ for 071213, and $(9.2 \pm 1.8) \times 10^{-2}$ cm$^{-2}$s$^{-1}$

217 for 081213. Then, multiplying these fluxes by the GEANT4-derived detection efficiency

218 for $\gamma$ rays of the plastic scintillator and the area of the plastic scintillator, 464 cm$^2$, $\gamma$-ray

219 produced counts contributing to $N_{pl}$ are estimated as $N_\gamma = 70 \pm 7$ for 071213, and $31 \pm 6$

220 for 081225. Finally, subtracting $N_\gamma$ from $N_{pl}$, the contribution of electrons is obtained as

221 $90 \pm 30$ for 071213, and $41 \pm 19$ for 081225. Although these numbers, when taken at their

222 face values, imply a significant electron contribution to $N_{pl}$, here we conservatively regard

them as upper limits. Then, a 95% confidence level upper limit on the electron flux above

1 MeV of 071213 and 081225 is computed as $0.5 \times 10^{-2}$ cm$^{-2}$s$^{-1}$ and $0.3 \times 10^{-2}$ cm$^{-2}$s$^{-1}$,

respectively. These upper limits are more than an order of magnitude lower than the

$1 - 10$ MeV $\gamma$-ray fluxes. Therefore, the observed burst signals arriving at the GROWTH

system are inferred to be dominated by photons, rather than electrons.

## 3.4. Comparison with signals from environmental sensors

The visible-light sensor (middle panels of Fig. 6) recorded an extremely intense signal,

lasting $\leq 1$ sec, at 15:57:50 UT and 9:25:09 UT, for 071213 and 081225, respectively. In

coincidence with the recorded optical flashes, the electric field rapidly changed its polarity

from positive to negative (bottom panels of Fig. 6). These indicate that a lightning

discharge occurred. However, their occurrence is well separated from the $\gamma$-ray bursts

themselves, namely, 100 sec and 180 sec prior to the 071213 and 082125 commencements,

respectively. Thus, we conclude that neither of the present two $\gamma$-ray bursts coincided

with lightning discharges.

Prior to the present work, *Tsuchiya et al.* [2007, 2009] have reported similar lack of

coincidence between prolonged $\gamma$-ray bursts and lightning discharges. In *Tsuchiya et al.*

[2007], a long-duration burst, lasting 40 sec, was detected by the GROWHT system 70 sec

prior to lightning, while in *Tsuchiya et al.* [2009], no lightning discharges were measured

over 5 minutes before or after a prolonged ($\sim 90$ sec) burst detected at a high-mountain

detector. These previously reported events, observed during thunderstorms, have also

been considered to be associated with thunderclouds.

In the same manner, we associate the present bursts with the thunderclouds, rather

than to lightning discharges. Actually, rainfall-thunder observation data[1], provided by

245  a laser observation system operated by Tokyo Electric Power Company, showed that

246  thunderclouds approached the Kashiwazaki-Kariwa nuclear plant from the sea side on

247  both occasions, and passed over it during the 10 minutes.

### 3.5.  Energy spectra

248  Figure 7 and Figure 8 show background-subtracted GROWTH spectra, obtained in the

249  burst periods of 071213 and 081225, respectively. In either case, we accumulated the data

250  over the burst period, and subtracted background spectra which were averaged over 10

251  minutes before and after the burst, although thunderstorms were ongoing during these

252  time periods. This is to remove $< 3$ MeV line-$\gamma$ rays induced mainly by radon decays,

253  which increase the background level by up to twice. To examine how the background

254  selection affects the final spectra (Figure 7 and Figure 8), we subtracted an alternative

255  background spectrum averaged over 5 minutes before and after the burst. However, the

256  background-subtracted spectra did not change by more than $\pm 10\%$ at $< 1$ MeV, or $\pm 5\%$

257  at $> 1$ MeV. These are almost negligible compared with the statistical errors.

258  In both events, the background-subtracted spectra of Detector-A and Detector-B exhibit

259  very hard continuum spectra, which clearly extend to 10 MeV. As shown in another

260  GROWTH event 070106 reported previously [*Tsuchiya et al.*, 2007], and in high-mountain

261  observations [*Torii et al.*, 2009; *Tsuchiya et al.*, 2009; *Chilingarian et al.*, 2010], similar

262  prolonged $\gamma$-ray emissions, extending to 10 MeV or higher, were observed, and have been

263  thought to be produced via bremsstrahlung. Thus, the present high-energy $\gamma$ rays must

264  also be produced via bremsstrahlung by electrons accelerated beyond 10 MeV. Given these

265  results, the present two events, together with the previous ones, may be understood as

266  manifestations of a common type of high-energy activity in thunderstorms.

As easily seen in Fig. 7 and Fig. 8, the obtained spectra, in particular those of Detector-B, flatten in $0.8 - 3$ MeV, even though they are not corrected for the detector responses. One of the causes of this flat is the Compton scattering: since the Compton scattering cross section in the atmosphere increases as photon energy decreases toward 0.1 MeV, photons at low energies would experience stronger Compton degradation than higher-energy ones.

### 3.6. Model fits

Supposing that the burst $\gamma$ rays were produced in a source located at a certain distance and propagated through atmosphere to reach our detectors, we may deduce the initial photon spectrum at the source, and estimate the source distance, from the background-subtracted spectra. Since the Detector-A spectra are complicated due to the passive and active shielding effects by the BGO well, below we analyze the Detector-B spectra. According to numerical calculations [*Roussel-Dupré et al.*, 1994; *Roussel-Dupré and Gurevich*, 1996; *Lehtinen et al.*, 1999; *Babich et al.*, 2007], an energy distribution function of runaway electrons, generated under the RREA mechanism, is expressed by a power-law function, or more precisely, an exponentially cut-off power-law. Consequently, we assume an initial photon number spectrum as

$$f(\epsilon_\mathrm{p}) = \alpha \epsilon_\mathrm{p}^{-\beta} \exp\left(-\epsilon_\mathrm{p}/\epsilon_\mathrm{c}\right) \ (\mathrm{MeV}^{-1}\mathrm{sr}^{-1}). \tag{1}$$

Here, $\alpha$ and $\beta$ are a normalization factor and a photon index, respectively, while $\epsilon_\mathrm{p}$ and $\epsilon_\mathrm{c}$ describe the emitted photon energy and a cut-off energy in MeV, respectively. While this equation represents an exponentially cut-off power law, it can also express a pure power-law by requiring $\epsilon_\mathrm{c} \to \infty$.

276   Below, let us estimate the source distance $d$ from our Detector-B data, as well as $\alpha$,

277   $\beta$, and $\epsilon_c$. In order to simulate the photon propagation in the atmosphere, we utilize

278   EGS4 [*Nelson et al.*, 1985] embedded in CORSIKA 6.500 [*Heck et al.*, 1998]. In the

279   CORSIKA simulation, the atmosphere consists of $N_2$, $O_2$, and Ar with the mole ratios

280   of 78.1%, 21.0%, and 0.9%, respectively. The density of the atmosphere, divided into 5

281   layers, depends exponentially on the altitude $h$, with a form of $A + B \exp\left(-h/C\right)$, with

282   $A, B, C$ being model parameters. For example, at $h < 4$ km, the model is specified as

283   $A = -186.6 \, \mathrm{g\,cm^{-2}}$, $B = 1222.7 \, \mathrm{g\,cm^{-2}}$, and $C = 9.94$ km [*Heck and Pierog*, 2009].

284   In addition, EGS4 can adequately treat electromagnetic processes in the relevant energy

285   range of a few tens of keV to a few tens of MeV.

286   Mono-energetic photon simulations were carried out for 33 incident energies from 50

287   keV to 100 MeV. The energy interval is set to 10 keV for 50 keV $-$ 90 keV, 100 keV for

288   100 keV $-$ 1 MeV, 1 MeV for 1 MeV $-$ 10 MeV, and 10 MeV for 10 MeV $-$ 100 MeV.

289   For one mono-energetic photon simulation, one million photons were vertically injected

290   to the atmosphere from a fixed source distance. In reality, 20 source distances from 20 m

291   to 2000 m were applied for one mono-energetic simulation. Then, we saved the energy,

292   angle, and species of all of photons and particles that arrive at the observatory level (40

293   m above sea level).

294   Figure 9 indicates three representative sets of simulated photon spectra, propagating

295   over $d = 300$ m $(36 \, \mathrm{g\,cm^{-2}})$, 1000 m $(120 \, \mathrm{g\,cm^{-2}})$, and 2000 m $(220 \, \mathrm{g\,cm^{-2}})$, with the

296   numbers in parentheses giving air mass calculated by the above exponential formula.

297   Punch-through photons, which suffer no interactions with air molecules, appear as a

298   strong peak at the highest end of each photon spectrum, while scattered ones form a

continuum toward lower energies. As the distance increases, the punch-through photons

and the scattered continuum are both strongly attenuated, in particular toward lower

energies, due primarily to Compton scattering. For instance, the survival probability for

10 (1) MeV punch-through photons to propagate over $d = 2000$ m is only 0.02 ($10^{-5}$)

times that over $d = 300$ m. Note that as discussed later in Sec. 4.3, a long-duration

burst probably changes in the burst period its viewing angle relative to a beam axis of

electrons accelerated in thunderclouds. Thus, the calculated photon spectra here would

vary according to the changes, and hence they will be treated in this work as ones averaged

over different viewing angles.

Convolving the simulated photon spectra with the detector responses, we can obtain

a model-predicted spectrum to be observed by the NaI and CsI scintillators. Finally,

we convolve these model predictions with the assumed source photon spectrum, eq.(1),

and fit the predictions simultaneously to the background-subtracted NaI and CsI spectra

(right panels of Fig. 7 and Fig. 8). Then, the model parameters, such as $\alpha$, $\beta$ and $\epsilon_c$, can

be determined so as to minimize the fit $\chi^2$.

Shown in Figure 10 are three representative model fits to the spectra of 071213 and

081225, assuming a power-law model. The choice of $d$ of 300, 1000, and 2000 m in

Fig. 10, respectively gave $\chi^2$ values as 48.4, 77.5, and 116 for 071213, and 40.9, 46.7, and

51.4 for 081225. By changing $d$ and repeating the fitting, we obtained $\chi^2$ curves as shown

in Figure 11, together with the $\chi^2$ minima as 46.5 at $d = 400$ m for 071213, and 40.9 at

$d = 300$ m for 081225. From these figure, we can constrain source distance. Table 2 and

Table 3 summarize the best-fit parameters for 071213 and 081225, respectively, together

with the constrained source distance. Also, low-energy parts ($< 300$ keV) of the two

spectra are found to play an important role to determine $d$. If we use the background

averaged over the 5 min intervals (instead of 10 min), the source distances become 350 m

for 071213, and 300 m for 081225. Thus, the distance is not affected significantly by the

systematic background uncertainty.

The NaI and CsI spectra have been explained, in either event, by a common set of model

parameters, although the fits are not necessarily good enough. The cut-off energy $E_c$ was

constrained to be rather high with relatively large errors. Thus, our data do not provide

evidence for spectral cut-off in either event. In agreement with this, the two spectral

models, a power law and an exponentially cut-off power law, gave similar goodness of fits

in both events. Importantly, the source distance have been constrained with a reasonable

accuracy.

As another attempt, we tentatively fixed $E_c$ at 7 MeV, which is the expected average

kinetic energy of runaway electrons (not of bremsstrahlung photons), and repeated the

model fitting. Then, the fit became worse in both events (4th column of Table 2 and

Table 3). Therefore, the initial photon spectrum is again inferred to extend beyond $\sim 7$

MeV.

## 4. Discussion

### 4.1. Source heights

Assuming a power-law function at the source, the $\gamma$-ray spectra of 071213 and 081225

suggest that the sources are located at $290 - 560$ m ($35 - 67 \, \mathrm{g \, cm^{-2}}$) and $120 - 690$ m

$(14 - 82 \, \mathrm{g \, cm^{-2}})$ above our system, respectively, both at 90% confidence level. In fact,

these constraints are in good agreement with the known heights of winter thunderclouds in

this area. Winter thunderclouds and winter lighting observed at the coastal area of Japan

Sea exhibit many features that have hardly been found from those in summer seasons and/or in other areas (e.g. *Rakov and Uman* [2005] and references therein). These include rather low altitudes of the development of these thunderclouds. Actually, *Goto and Narita* [1992] conducted video observations of winter lightning at the same Niigata Prefecture as our experimental site, and reported that the visible bases of winter thunderclouds are typically located at 200 m − 800 m above sea level. Also, a recent numerical calculation done by *Babich et al.* [2010] shows that another GROWTH event [*Tsuchiya et al.*, 2007] may be produced at a source height of 0.5 − 2 km, and hence generally agrees with the present results.

These height estimations provide an additional clue to the possible electron contributions to the detected plastic signals (Sec. 3.3). As argued so far, electrons are considered to be accelerated in these thunderclouds to at least 10 MeV, probably a few tens of MeV. Since such electrons have a range of $< 100$ m at near the sea level, they would hardly reach our system, even if a range straggling is taken into account. Therefore, it is reasonable that the electron flux incident on our system, if any, was much lower than that of photons.

Unlike the present sea-level observations, some high-mountain experiments, conducted at Mt. Norikura (2770 m) in Japan [*Tsuchiya et al.*, 2009] and Mt. Aragatz (3250 m) in Armenia [*Chilingarian et al.*, 2010], have detected primary electrons in long duration events (numbers in parentheses indicate altitudes of observatories). *Tsuchiya et al.* [2009] estimated the source height as 60 − 130 m (90% confidence level), while *Chilingarian et al.* [2010] evaluated it as 100 − 150 m. These low source heights, which are comparable to or shorter than the expected electron range, can naturally explain their electron detections.

## 4.2. Extent and motion of the $\gamma$-ray beams

365    Measuring electric-field structure of winter thunderclouds, *Kitagawa and Michimoto*

366  [1994] revealed that tripole electrical structures, which consist of positive, negative and

367  positive layers from top to bottom, appear at mature stages of winter thunderclouds.

368  Then, they observed the tripole structures to last for < 10 minutes in early or late winter,

369  while less than several minutes in midwinter. Since the present two events were observed

370  in midwinter, the measured burst periods of 84 sec of 071213 and 72 sec of 081225 are

371  consistent with their observations, if the burst durations represent the lifetime of electric

372  fields.

373    Figure 12 shows dose variations on 2007 December 13, measured by the nearest and the

374  second nearest radiation monitors of the power plant (5 and 6 in Fig. 1, black and red lines

375  in Fig. 12, respectively). The two monitors gave moderate dose increases for $\sim 1$ minute

376  or less around the GROWTH event. By examining the GROWTH data of 071213 burst

377  (crosses in Fig. 12), as well as dose rates of the second nearest monitor (red line) obtained

378  for $15:59:30 - 16:01:00$ UT and that of the nearest one (black line) obtained over $16:00:00$

379  $- 16:01:30$ UT, peak times of their enhancement can be evaluated as $15:59:48$ ($\pm 6$ sec)

380  UT, $15:59:58$ ($\pm 15$ sec) UT, and $16:00:27$ ($\pm 15$ sec) UT. Thus, referring to the GROWTH

381  data, the second nearest monitor increased in its dose rates with a small delay of $10 \pm 16$

382  sec (or almost simultaneously), while the nearest one with a larger delay by $39 \pm 16$ sec.

383  The two monitors are located at a distance of $500 - 600$ m from the GROWTH system.

384  For reference, data of the other two radiation monitors (4 and 7 in Fig. 1) exhibited no

385  apparent increases (green and blue lines in Fig. 12). As for 081225, data of those radiation

386  monitors were unavailable due to some data-storage problem.

These simultaneous and delayed detections by the two radiation monitors have two important implications. One is that the $\gamma$-ray emission from thunderclouds is likely to have illuminated a rather limited area, spreading over $\sim 600$ m on the ground. This kind of effect was also suggested by five radiation monitors ($1-5$ in Fig. 1), on the occasion of the other GROWTH event [*Tsuchiya et al.*, 2007], and another experiment conducted on the same coastal area [*Torii et al.*, 2002]. The other is that the $\gamma$-ray emitting region moved, presumably together with the thunderclouds.

From data of Japan Meteorological Agency, it is found that south-west wind was blowing during 10 minutes including the burst period of 071213. Thus, the south-west direction can naturally explain the delay of the nearest monitor, if the $\gamma$-ray emitting region moved together with the thunderclouds. Then, the wind velocity was on average $360\,\mathrm{m\,min^{-1}}$, with the maximum of $720\,\mathrm{m\,min^{-1}}$. Projecting, to south-west axis, the distance between the GROWTH system and the nearest monitor, $\sim 500$ m, and dividing the projected distance, $\sim 350$ m, by its delay, $39 \pm 16$ sec, we obtain an average moving velocity of the emitting region as $540 \pm 220\ \mathrm{m\,min^{-1}}$. Thus, the estimated moving velocity is generally consistent with the wind velocity.

Given above discussions, we may assume that the winter thunderclouds moved from the Japan sea in south-west side to the inland in north-east side. Then, a short-lived tripole structure appeared in a thundercloud, and accelerated ambient fast electrons toward the bottom positive layer. The accelerated electrons emitted $\gamma$ rays toward the ground, which the GROWTH system and the two radiation monitors detected when the beam passed over them. The differences in the statistical significance of detections between the GROWTH system and the radiation monitors may be due to different positions and effective viewing

410  angles relative to the accelerated electron beam axis in the thundercloud, and to the

411  differences in their sensitivity. The 081225 event is considered to have occurred under

412  similar conditions, because west winds, with almost the same velocity as in the 071213

413  case, were blowing at that time. However, it is presently unclear whether the $\gamma$-ray

414  emission ceased when the tripole structure disappeared, or when the $\gamma$-ray beam moved

415  away from the GRWOTH system as the thunderclouds moved.

## 4.3.  The number of relativistic electrons in thunderclouds

Using the initial photon energy spectrum $f(\epsilon_{\mathrm{p}})$ of Eq. (1) as quantified in Table 2

and Table 3, we can estimate the number of relativistic electrons radiating the observed

$1 - 10\,\mathrm{MeV}$ $\gamma$ rays via bremsstrahlung, as

$$N_{\mathrm{e}} \sim \frac{2\pi}{H} \int_{1}^{10} dK_{\mathrm{e}} \int_{1}^{K_{\mathrm{e}}} d\epsilon_{\mathrm{p}} \int_{0}^{\theta_{\max}} \frac{f(\epsilon_{\mathrm{p}})}{\eta(K_{\mathrm{e}}, \epsilon_{\mathrm{p}}, \theta)} \sin\theta d\theta. \tag{2}$$

416  Here, $\eta(K_{\mathrm{e}}, \epsilon_{\mathrm{p}}, \theta)$ is the probability per $1\ \mathrm{g\,cm^{-2}}$ with which an electron with a kinetic

417  energy $K_{\mathrm{e}}$ emits a bremsstrahlung photon with an energy $\epsilon_{\mathrm{p}}$ at an angle $\theta$ with respect

418  to the electron-beam axis [*Koch and Motz*, 1959], and $H$ denotes the vertical length of

419  the acceleration region. Since this $H$ is unavailable from the present observations like in

420  *Tsuchiya et al.* [2009], we assume either $H = 300$ m or 1000 m, corresponding to $35\,\mathrm{g\,cm^{-2}}$

421  and $110\,\mathrm{g\,cm^{-2}}$, respectively. These assumptions are based on intracloud observations of

422  X rays using a ballon-born detector, which showed that a high electric field region, to

423  produce a significant flux in $3 - 120$ keV energy range, has a vertical extent of $\sim 500$ m,

424  at altitudes of $3.7 - 4.2$ km [*Eack et al.*, 1996].

425  We further assumed that the electric-filed strength in the acceleration region is 300

426  kV m$^{-1}$, which is slightly higher than the threshold (at 1 atm) to cause the runaway elec-

tron avalanches. When 1 MeV electrons are accelerated from the top of this acceleration region to the bottom, they will gain energies of 15 MeV for $H = 300$ m, and 19 MeV for $H = 1000$ m. Therefore, the assumed electric-field strength, together with the assumed vertical length, is sufficient to produce 10 MeV photons via bremsstrahlung.

To calculate eg.(2), we further need to specify $\theta$; this is suggested to be relatively small, from the obtained photon spectra. In practice, the angle of prolonged $\gamma$-ray event may vary according to the motion of thunderclouds. Thus, we adopt 15° or 30° as $\theta_{\mathrm{max}}$. As listed in Table 4, these assumptions, together with eq. (1), give $N_{\mathrm{e}} = 10^9 - 10^{11}$. Similar estimations for other long-duration $\gamma$-ray bursts have given $N_{\mathrm{e}} = 10^8 - 10^{12}$ [*Tsuchiya et al.*, 2007, 2009; *Chilingarian et al.*, 2010]. Thus, long-duration $\gamma$-ray bursts appear to be emitted by a similar number of relativistic electrons.

## 4.4. Relation between the bursts and the RREA mechanism

A possible source of energetic seed electrons to cause the RREA can be attributable to secondary cosmic rays [*Gurevich et al.*, 1992]. The cosmic-ray flux above 1 MeV, at the presently relevant altitudes of <1 km, is $I_0 \sim 200\,\mathrm{m^{-2}s^{-1}}$ [*Grieder*, 2001]. Considering the measured burst periods of $70 - 80$ sec and the $30 - 40$ sec delay of one radiation monitor from the 071213 event, we presume that the acceleration region has a horizontal length of $L \sim 600$ m at most, as judged from the extent of the $\gamma$-ray beam of 071213. Possibly, an actual extent of the acceleration region in thunderclouds would be shorter than this 600 m, because the $\gamma$-ray beam would diverge due to multiple scatterings of the emitting electrons and Compton scatterings of the emitted $\gamma$ rays. We may also consider that an acceleration region is sustained in thunderclouds at least for 100 sec. Accordingly, the

number of cosmic rays $S_0$, entering the acceleration region, is described as

$$S_0 = 7.2 \times 10^9 \times (L/600 \text{ m})^2 \times \Delta t/100 \text{ sec.} \qquad (3)$$

Based on the RREA mechanism, the total number of relativistic electrons at the end of

an acceleration region, $N_{\text{RREA}}$, is estimated as

$$N_{\text{RREA}} = S_0 \exp(\delta), \ \delta = \int_0^H \frac{dz}{\lambda}. \qquad (4)$$

The length parameter $\lambda$ is given as

$$\lambda = \frac{7300 \text{ kV}}{E - (276 \text{ kV m}^{-1})n} \text{ m,} \qquad (5)$$

where $E$ is the electric-field strength in $\text{kV m}^{-1}$ and $n$ denotes the air density relative to

that at 1 atm. This formula is valid for $300 - 3000 \text{ kV m}^{-1}$ [*Dwyer*, 2003]. Assuming

$E = 300 \text{ kV m}^{-1}$ gives $\lambda \sim 300 \text{ m}$ at $P = 1$ atm. In practice, $E$ may be somewhat lower

than $300 \text{ kV m}^{-1}$, because $P$ during thunderstorms would be usually lower than 1 atm

due to lower pressure system, and hence gives $n < 1$. Since a uniform field, $\delta = H/\lambda$,

gives $N_{\text{RREA}} = S_0 \exp(H/\lambda)$, the factor $\eta = \exp(H/\lambda)$ is regarded as the avalanche

multiplication factor, and becomes 3 and 30 for $H = 300$ m and 1000 m, respectively. As

a result, we obtain

$$N_{\text{RREA}} = 2.2 \times 10^{11} \times (L/600 \text{ m})^2 \times \Delta t/100 \text{ sec} \times \eta/30. \qquad (6)$$

We thus obtain $N_{\text{RREA}} = 10^{10} - 10^{11}$, which agrees generally with the derived $N_e = 10^9 - 10^{11}$. Thus, the standard RREA process can explain at least the present two prolonged bursts.

In the above estimation, we assumed an electric field is slightly higher than the RREA

threshold. However, a weaker field below this threshold might suffice to produce prolonged

γ-ray emission. In reality, a $30 - 120$ keV x-ray flux continuously increased while an electric field is lower by $30\% - 60\%$ than the RREA threshold [*Eack et al.*, 1996]. This quasi-static moderate-level field might be accomplished by e.g. a charging mechanism of thunderclouds.

## 4.5.  Comparisons with TGFs

The derived $N_e$ (sec.4.4) is more than five orders of magnitude lower than the number of relativistic electrons expected from TGF observations, e.g. $10^{16} - 10^{17}$ [*Dwyer and Smith*, 2005]. This huge number of relativistic electrons in TGFs may be generated by relativistic feedback mechanism, involving positrons and X rays propagating in the opposite direction to runaway electrons [*Dwyer*, 2007, 2008]. Since the estimated $N_e$ of the present bursts is in generally agreement with $N_{\mathrm{RREA}}$ expected from the simple RREA mechanism, we conclude that at least the present two events do not require an intense feedback process.

In order to better characterize γ-ray spectra of long-duration events, we stacked count spectra over three bursts, namely, the present two ones and 070106 [*Tsuchiya et al.*, 2007]. Figure 13 compares the summed GROWTH spectrum with averaged TGF ones obtained by two independent satellites; one sums 289 events measured by Reuven Ramaty High Energy Solar Spectroscopic Imager (RHESSI) [*Dwyer and Smith*, 2005], while the other averages over 34 events observed by the Astrorivelatore Gamma a Immagini Leggero (AGILE) satellite [*Marisaldi et al.*, 2010a]. Thus, the composite GROWTH spectrum is rather similar in shape to those from TGFs, although three spectra all include detector responses. This resemblance is consistent with our basic standpoint [*Tsuchiya et al.*, 2007, 2009] that the long-duration γ rays are emitted by the same bremsstrahlung process as TGFs.

On a close comparison, the TGF spectra, especially the AGILE one, appear to have a higher cut-off energy than the GROWTH spectrum. This may be attributable to a difference in the electric potential operating in an acceleration region [*Dwyer and Smith*, 2005]. Thus, electrons accelerated in a much lower atmospheric density at the production sites of TGFs, $15 - 40$ km [*Dwyer and Smith*, 2005; *Carlson et al.*, 2007; *Østgaard et al.*, 2008], would propagate through a longer distance, which gives a higher electric potential, and gain higher energies because of a smaller ionization loss per unit length.

## 5. Summary

The GROWTH experiment observed two long-duration $\gamma$-ray emissions from winter thunderstorms on 2007 December 13 and 2008 December 25. The photon spectra obtained in both events clearly extends to 10 MeV, and are consistent with a scenario that accelerated electrons produce, via bremsstrahlung, the observed $\gamma$ rays. Adopting a power-law function as the initial photon spectrum at the source, we have constrained the source distance as $290 - 560$ m for 071213 and $110 - 690$ m for 081225, both at 90% confidence level. These constraints agree with visible-light observations, which show that the bottom of winter thunderclouds is usually located at $200 - 800$ m above sea level [*Goto and Narita*, 1992]. We have shown a possibility that the observed $\gamma$-ray beams move with winter thunderclouds, and spread over $\sim 600$ m.

We estimated the number of relativistic electrons to cause the present prolonged $\gamma$-ray emissions as $10^9 - 10^{11}$. These are in general agreement with those expected from the standard RREA mechanism triggered by secondary cosmic rays. The cumulative GROWTH spectrum, summed over the present two ones and another GROWTH event [*Tsuchiya*

et al., 2007], was found to be similar in basic spectral features with the averaged TGF

spectra [*Dwyer and Smith*, 2005; *Marisaldi et al.*, 2010a].

## Notes

1. raifall-thunder observation data are available from http://thunder.tepco.co.jp/

## References

Agostinelli, S., et al., (2003), Geant4a simulation toolkit, *Nucl. Inst. Meth. A 506*, 250, doi:10.1016/S0168-9002(03)01368-8.

Alexeenko, V. V., N. S. Khaerdinov, A. S. Lidvansky, and V. B. Petkov (2002), Transient variations of secondary cosmic rays due to atmospheric electric field and evidence for pre-lightning particle acceleration, *Phys. Lett. A 301*, 299, doi:10.1016/S0375-9601(02)00981-7.

Babich, L. P., E. N. Donskoi, R. I. Ilkaev, I. M. Kutsyk, and R. A. Roussel-Dupré (2004), Fundamental parameters of a relativistic runaway electron avalanche in air, *Plasm. Phys. Rep. 30*, 616, doi:10.1134/1.1778437.

Babich, L. P., E. N. Donskoi, I. M. Kutsyk, and R. A. Roussel-Dupré (2005), The feedback mechanism of runaway air breakdown, *Geophys. Res. Lett. 32*, L09809, doi:10.1029/2004GL021744.

Babich, L. P., E. N. Donskoy, and R. A. Roussel-Dupré (2007), Study of relativistic electron avalanche enhancement in the atmosphere at low overvoltages due to avalanche bremsstrahlung, *Geomag. and Aeron. 47*, 515, doi:10.1134/S0016793207040135.

Babich, L. P., E. I. Bochkov, E. N. Donskoi, and I. M. Kutsyk (2010), Source of prolonged bursts of high-energy gamma rays detected in thunderstorm atmosphere in Japan at the coastal area of the Sea of Japan and on high mountaintop, *J. Geophys. Res.*, *115*, A09317, doi:10.1029/2009JA015017.

Bell, T. F., V. P. Pasko, and U. S. Inan (1995), Runaway electrons as a source of Red sprites in the mesosphere, *Geophys. Res. Lett. 22*, 2127, doi:10.1029/95GL02239.

Briggs, M. S., et al. (2010), First results on terrestrial gamma ray flashes from the Fermi Gammaray Burst Monitor, *J. Geophys. Res.*, *115*, A07323, doi:10.1029/2009JA015242.

Brunetti, M., S. Cecchini, M. Galli, G. Giovannini, and A. Pagliarin (2000), Gamma-ray bursts of atmospheric origin in the MeV energy range, *Geophys. Res. Lett. 27*, 1599, doi:10.1029/2000GL003750.

Carlson, B. E., N. G. Lehtinen, and U. S. Inan (2007), Constraints on terrestrial gamma ray flash production from satellite observation, *Geophys. Res. Lett. 34*, L08809, doi:10.1029/2006GL029229.

Chilingarian, A., A. Daryan, K. Arakelyan, A. Hovhannisyan, B. Mailyan, L. Melkumyan, G. Hovsepyan, S. Chilingaryan, A. Reymers, and L. Vanyan (2010), Ground-based observations of thunderstorm-correlated fluxes of high-energy electrons, gamma rays,

and neutrons, *Phys. Rev. D 82*, 043009, doi:10.1103/PhysRevD.82.043009.

Chubenko, A. P. et al. (2000), Intensive X-ray emission bursts during thunderstorms, *Phys. Lett. A 275*, 90, doi:10.1016/S0375-9601(00)00502-8.

Chubenko, A. P. et al. (2009), Energy spectrum of lightning gamma emission, *Phys. Lett. A 373*, 2953, doi:10.1016/j.physleta.2009.06.031.

Connaughton, V. et al. (2010), Associations between Fermi Gamma-ray Burst Monitor terrestrial gamma ray flashes and sferics from the World Wide Lightning Location Network, *J. Geophys. Res. 115*, A12307, doi:10.1029/2010JA015681.

Dwyer, J. R. (2003), A fundamental limit on electric fields in air, *Geophys. Res. Lett. 30*, 2055, doi:10.1029/2003GL017781.

Dwyer, J. R. et al. (2003), Energetic radiation produced during rocket-triggered lightning, *Science 299*, 694, doi:10.1126/science.1078940.

Dwyer, J. R et al. (2004a), Measurements of x-ray emission from rocket-triggered lightning, *Geophys. Res. Lett. 31*, L05118, doi:10.1029/2003GL018770.

Dwyer, J. R. et al. (2004b), A ground level gamma-ray burst observed in association with rocket-triggered lightning, *Geophys. Res. Lett. 31*, L05119, doi:10.1029/2003GL018771.

Dwyer, J. R. (2004c), Implications of x-ray emission from lightning, *Geophys. Res. Lett.*, *31*, L12102, doi:10.1029/2004GL019795.

Dwyer, J. R. et al. (2005), X-ray bursts associated with leader steps in cloud-to-ground lightning, *Geophys. Res. Lett. 32*, L01803, doi:10.1029/2004GL021782.

Dwyer, J. R., and D. M. Smith (2005), A comparison between Monte Carlo simulations of runaway breakdown and terrestrial gamma-ray flash observations, *Geophys. Res. Lett. 32*, L22804, doi:10.1029/2005GL023848.

Dwyer, J. R. (2007), Relativistic breakdown in planetary atmosphere, *Phys. Plasm. 14*, 04290, doi:10.1063/1.2709652.

Dwyer, J. R. (2008), Source mechanisms of terrestrial gamma-ray flashes, *J. Geophys. Res. 113*, D10103, doi:10.1029/2007JD009248.

Eack, K. B., W. H. Beasley, R. W. David, T. C. Marshall, and M. Stolzenburg (1996), Initial results from simultaneous observation of X rays and electric fields in a thunderstorms, *J. Geophys. Res. D23*, 29637, doi:10.1029/96JD01705.

Eack, K. B., D. M. Suszcynsky, W. H. Beasley, R. Roussel-Dupre, and E. Symbalisty (2000), Gamma-ray emissions observed in a thunderstorm anvil, *Geophys. Res. Lett. 27*, 185, doi:10.1029/1999GL010849.

Enoto, T., H. Tsuchiya, S. Yamada, T. Yuasa, M. Kawaharada, T. Kitaguchi, M. Kokubun, H. Kato, M. Okano, S. Nakamura, and K. Makishima (2007), Detection of gamma-rays from winter thunderclouds along the coast of Japan Sea, *Proc. 30th Int. Cosmic Ray. Conf.* .

Fishman, G. J. et al. (1994), Discovery of intense gamma-ray flashes of atmospheric origin, *Science 264*, 1313, doi:10.1126/science.264.5163.1313.

Goto, Y., and K. Narita, (1992), Observations of winter lightning to an isolate tower, *Res. Lett. Atmos. Electr. 12*, 57.

Grefenstette, B. W., D. M. Smith, B. J. Hazelton, and L. I. Lopez (2009), First RHESSI terrestrial gamma ray flash catalog, *J. Geophys. Res 114*, A02314, doi:10.1029/2008JA013721.

Grieder, P. K. F. (2001), *Cosmic rays at earth* pp. 198−230, Elsevier Science B. V., Amsterdam.

Gurevich, A. V., G. M. Milikh, and R. A. Roussel-Dupré (1992), Runaway electron mechanism of air breakdown and preconditioning during a thunderstorm, *Phys. Lett. A 165*, 463, doi:10.1016/0375-9601(92)90348-P.

Gurevich, A. V., G. M. Milikh, and J. A. Valdivia (1997), Model of X-ray emission and fast preconditioning during a thunderstorm, *Phys. Lett. A 231*, 402, doi:10.1016/S0375-9601(97)00354-X.

Gurevich, A. V., K. P. Zybin, and Yu. V. Medvedev (2007), Runaway breakdown in strong electric field as a source of terrestrial gamma flashes and gamma bursts in lightning leader steps, *Phys. Lett. A 361*, 119, doi:10.1016/j.physleta.2006.05.063.

Heck, D. et al., (1998), Report FZKA 6019, Forschungszentrum Karlsruhe.

Heck, D., and T. Pierog, (2009), Extensive Air Shower Simulation with CORSIKA: A User's Guide, p.114, Forschungszentrum Karlsruhe,

Howard, J., M. A. Uman, J. R. Dwyer, D. Hill, C. Biagi, Z. Saleh, J. Jerauld, H. K. Rassoul (2008) Co-location of lightning leader x-ray and electric field change sources, *Geophys. Res. Lett. 35*, L13817, doi:10.1029/2008GL034134.

Kitagawa, N., and K. Michimoto (1994), Meteorological and electrial aspects of winter thunderclouds, *J. Geophys. Res. 99*, 10713, doi:10.1029/94JD00288.

Koch, H. W., and J. W. Motz (1959), Bremsstrahlung cross-section formulas and related data, *Rev. Mod. Phys. 31*, 920, doi:10.1103/RevModPhys.31.920.

Lehtinen, N. G., M. Walt, U. S. Inan, T. F. Bell, and V. P. Pasko (1996), $\gamma$-ray emission produced by a relativistic beam of runaway electrons accelerated by quasi-electrostatic thundercloud fields, *Geophys. Res. Lett. 23*, 2645, doi: 10.1029/96GL02573.

Lehtinen, N. G., T. F. Bell, and U. S. Inan (1999), Monte Carlo simulation of runaway MeV electron breakdown with application to red sprites and terrestrial gamma ray flashes, *J. Geophys. Res. 104*, 24699, doi:10.1029/1999JA900335.

Marisaldi, M., et al., (2010a), Detection of terrestrial gamma ray flashes up to 40 MeV by the AGILE satellite, *J. Geophys. Res. 115*, A00E13, doi:10.1029/2009JA014502.

Marisaldi, M., et al., (2010b), Gamma-Ray Localization of Terrestrial Gamma-Ray Flashes, *Phys. Rev. Lett. 105*, 128501, 10.1103/PhysRevLett.105.128501.

McCarthy, M. P., and G. K. Parks (1985), Further observations of x-rays inside thunderstorms, *Geophys. Res. Lett. 12*, 393, doi:10.1029/GL012i006p00393.

Milikh, G., and J. A. Valdivia (1999), Model of gamma ray flashes due to fractal lightning, *Geophys. Res. Lett. 26*, 525, doi:10.1029/1999GL900001.

Moore, C. B., K. B. Eack, G. D. Aulich, and W. Rison (2001), Energetic radiation associated with lightning stepped-leaders, *Geophys. Res. Lett. 28*, 2141, doi:10.1029/2001GL013140.

Muraki, Y. et al. (2004), Effects of atmospheric electric fields on cosmic rays, *Phys. Rev. D 69*, 123010, doi:10.1103/PhysRevD.69.123010.

Nelson, W. R., H. Hirayama, and D. W. O Rogers, *Report SLAC 265* (1985).

Østgaard, N., T. Gjesteland, J. Stadsnes, P. H. Connell, and B. Carlson (2008), Production altitude and time delays of the terrestrial gamma flashes: Revisiting the Burst and Transient Source Experiment spectra, *J. Geophys. Res. 113*, A02307, doi:10.1029/2007JA012618.

Rakov, V. A., and M. A. Uman (2005), Winter lightning in Japan in *Lightning Physics and Effects*, 3rd ed., pp. 308 - 320., Cambridge Univ. Press.

Roussel-Dupré, R. A., A. V. Gurevich, T. Tunnell, and G. M. Milikh (1994), Kinetic theory of runaway air breakdown, *Phys. Rev. E 49*, 2257, doi:10.1103/PhysRevE.49.2257.

Roussel-Dupré, R. A., and A. V. Gurevich (1996), On runaway breakdown and upward propagating discharges, *J. Geophys. Res. 101*, 2297, doi:10.1029/95JA03278.

Roussel-Dupré, R., J. J. Colman, E. Symbalisty, D. Sentman, and V. P. Pasko (2008), Physical Processes Related to Discharges in Planetary Atmosheres, *Space Sci. Rev. 137*, 51, doi:10.1007/s11214-008-9385-5.

Smith, D. M., L. I. Lopez, R. P. Lin, and C. P. Barrington-Leigh (2005), Terrestrial gamma-ray flashes observed up to 20 MeV, *Science 307*, 1085, doi:10.1126/science.1107466.

Suszcynsky, D. M., R., Roussel-Dupré, and C., Shaw (1996), Ground-based search for X rays generated by thunderstorms and lightning, *J. Geophys. Res. 101*, 23505, doi:10.1029/96JD02134.

Torii, T., M. Takeishi, and T. Hosono (2002), Observation of gamma-ray dose increase associated with winter thunderstorm and lightning activity, *J. Geophys. Res. 107*, 4324, doi:10.1029/2001JD000938.

Torii T.,T. Sugita, S. Tanabe, Y. Kimura, M. Kamogawa, K. Yajima, and H. Yasuda (2009), Gradual increase of energetic radiation associated with thunderstorm activity at the top of Mt. Fuji, *Geophys. Res. Lett. 36*, L13804, doi:10.1029/2008GL037105.

Tsuchiya, H. et al. (2007), Detection of high-energy gamma rays from winter thunderclouds, *Phys. Rev. Lett. 99*, 165002, doi:10.1103/PhysRevLett.99.165002

Tsuchiya, H. et al. (2009), Observation of an energetic radiation burst from mountain-top thunderclouds, *Phys. Rev. Lett. 102*, 255003, doi:10.1103/PhysRevLett.102.255003.

Yamazaki, K., S. Tonouchi, and T. Hashimoto (2002), Factors associated with the variations in environmental gamma-ray spectra in Kashiwazaki Kariwa area *J. Radio. Nucl. Chem. 252*, 359, doi:10.1023/A:1015734810119

Yoshida, S., T. Morimoto, T. Ushio, Z.-I Kawasaki, T. Torii, D. Wang, N. Takagi, and T. Watanabe (2008), High energy photon and electron bursts associated with upward lightning strokes, *Geophys. Res. Lett. 35*, L10804, doi:10.1029/2007GL032438.

Yoshioka, K. (1992), The seasonal variation of rainout activity of short-lived radon daughters, *Rad. Prot. Dosim. 45*, 395, doi:
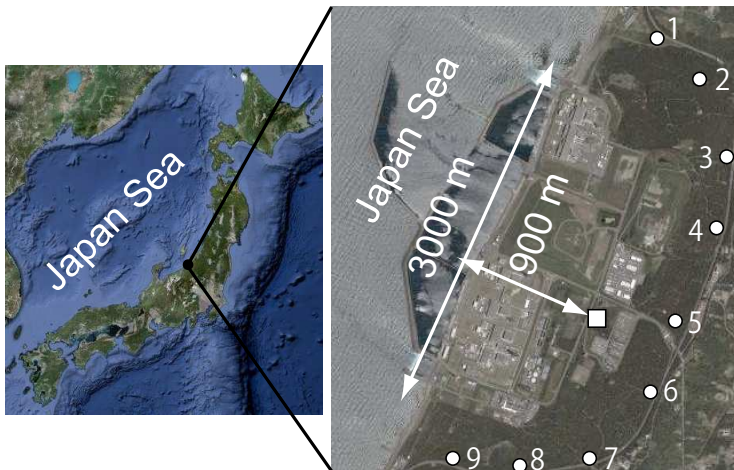
**Figure 1.**    The location of the Kashiwazaki-Kariwa nuclear power plant (left) and its bird view (right). A filled square in the right panel represents the GROWTH experimental site, while 9 filled circles show locations of radiation monitors. Each original image is taken from Google Map.
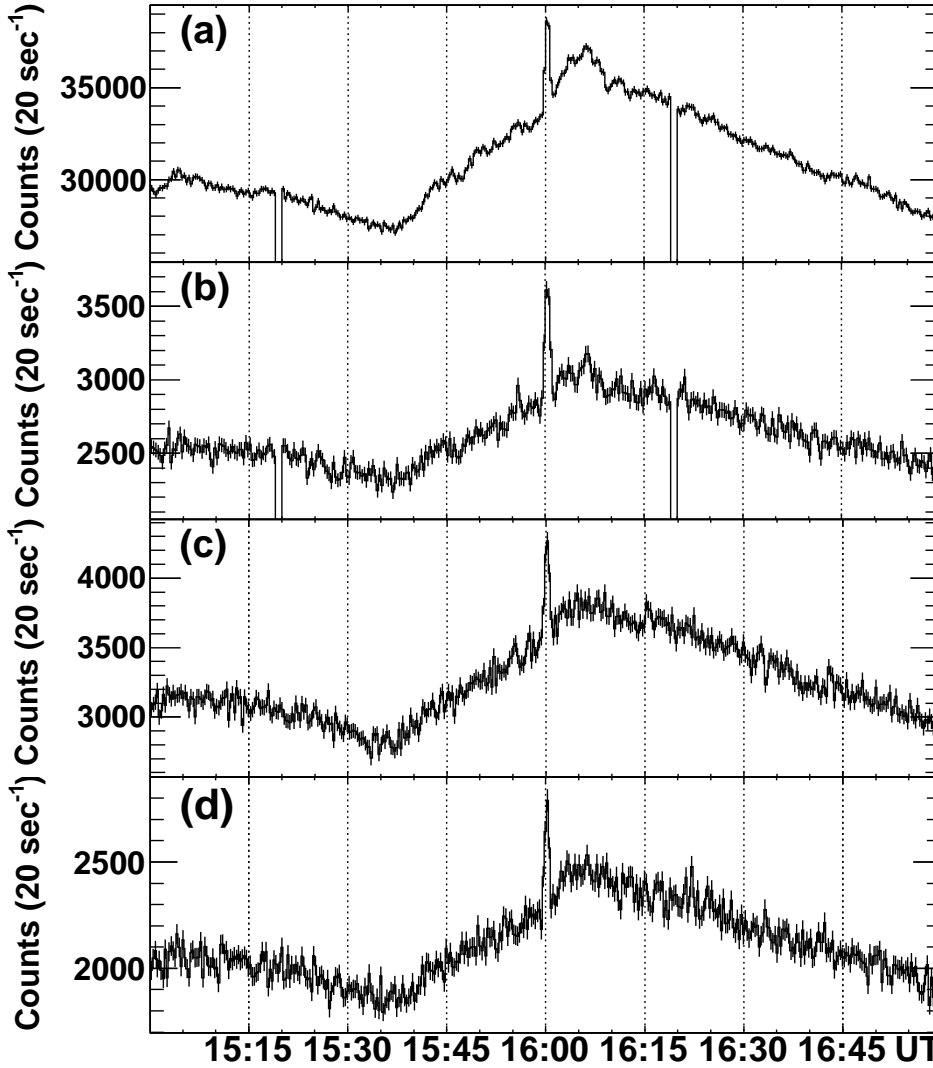
**Figure 2.**    Count rates per 20 sec of the 4 inorganic scintillators over $15:00 - 17:00$ UT on 2007 December 13. Panels (a) and (b) show the $> 40$ keV count rates from the BGO and NaI scintillators without the anticoincidence of Detector-A, respectively, while panels (c) and (d) represent those of NaI ($> 40$ keV) and CsI ($> 300$ keV) scintillators of Detector-B, respectively. Horizontal axis shows universal time. Error bars are statistical $1\sigma$. The gaps in panels (a) and (b) are due to regular interruptions of data acquisition of Detector-A every hour.
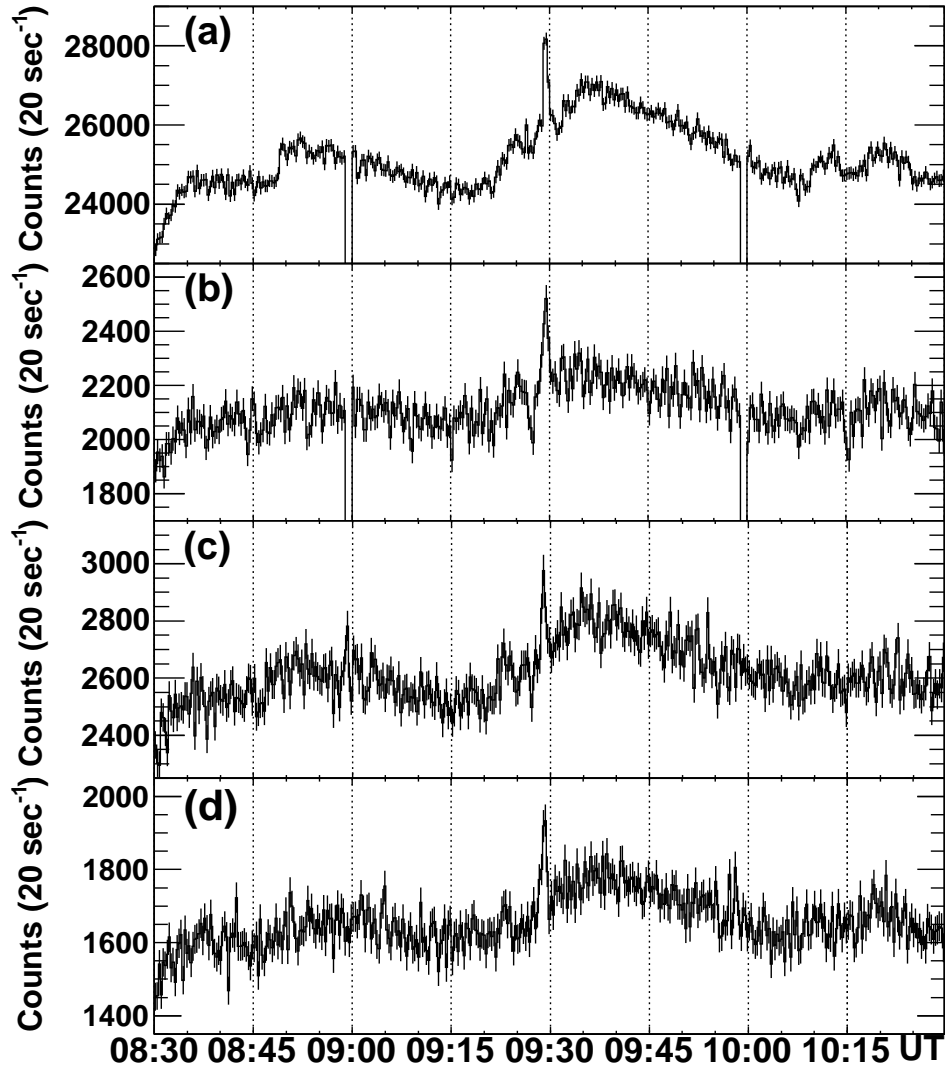
**Figure 3.**  The same as Fig. 2, but over 8:30 − 10:30 UT on 2008 December 25.
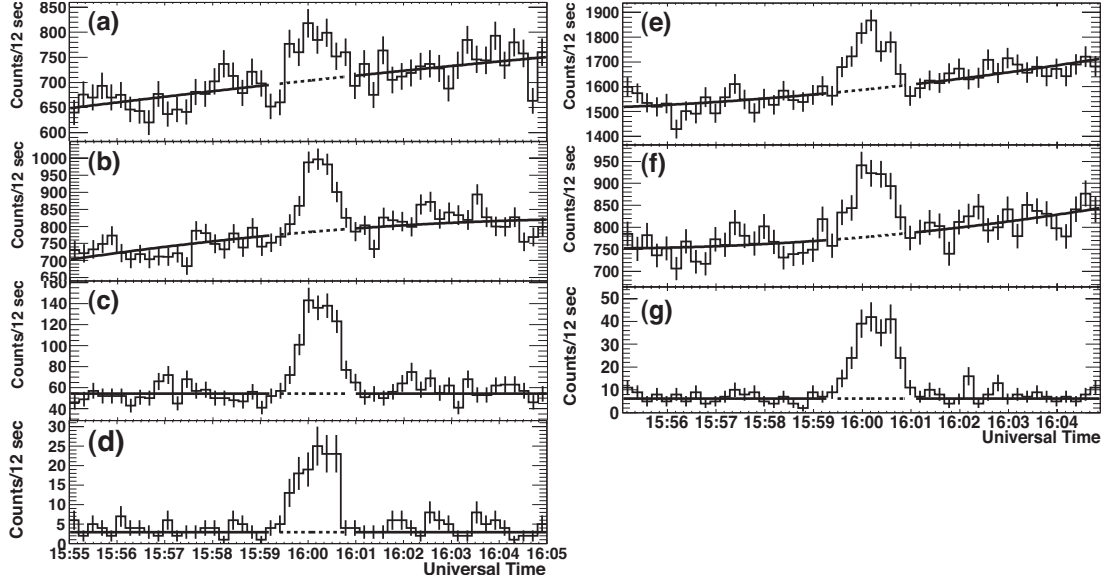
**Figure 4.**    Count histories per 12 sec of 071213 in three energy bands from Detector-A (left; summed over the two NaI) and Detector-B (right; NaI), obtained for $15:55 - 16:05$ UT. Panels (a), (b) and (c) correspond to $0.04 - 0.3$ MeV, $0.3 - 3$ MeV and $> 3$ MeV energy bands without anticoincidence, respectively.  Panel (d) indicates the $> 3$ MeV energy band of the NaI with anticoincidence.  Panels (e), (f) and (g) are the same as Panels (a), (b) and (c), respectively, but for Detector-B. Solid curves outside the burst period show the estimated background level (see text), while dashed ones denote the interpolated background level over the burst period. Abscissa represents universal time. Each error bar is statistical $1\sigma$.
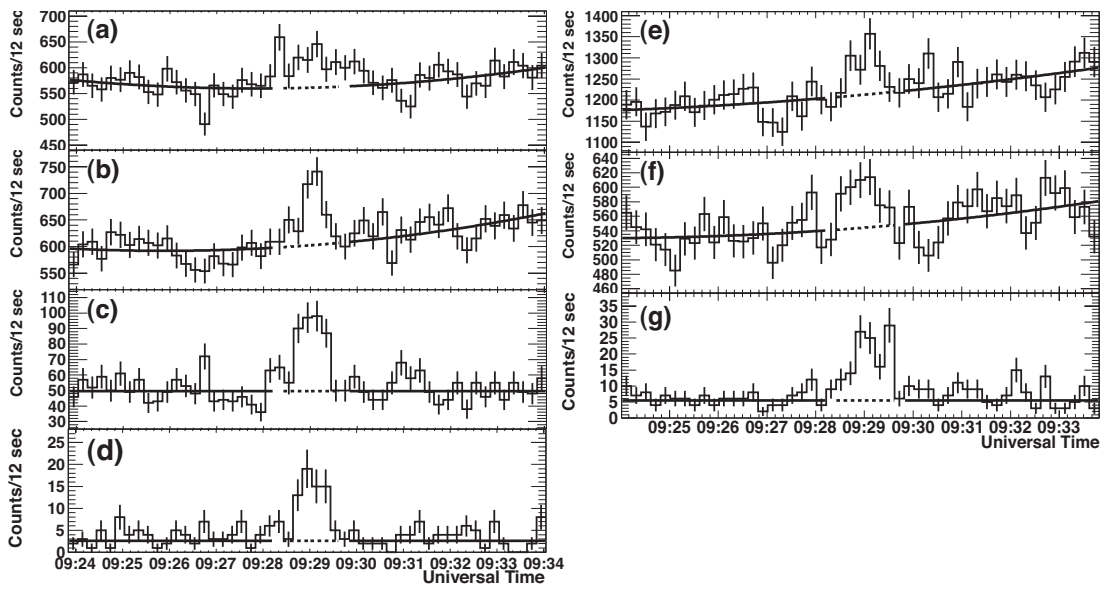
**Figure 5.**   The same as Fig. 4, but for 081225, obtained over $9{:}24 - 9{:}34$ UT.
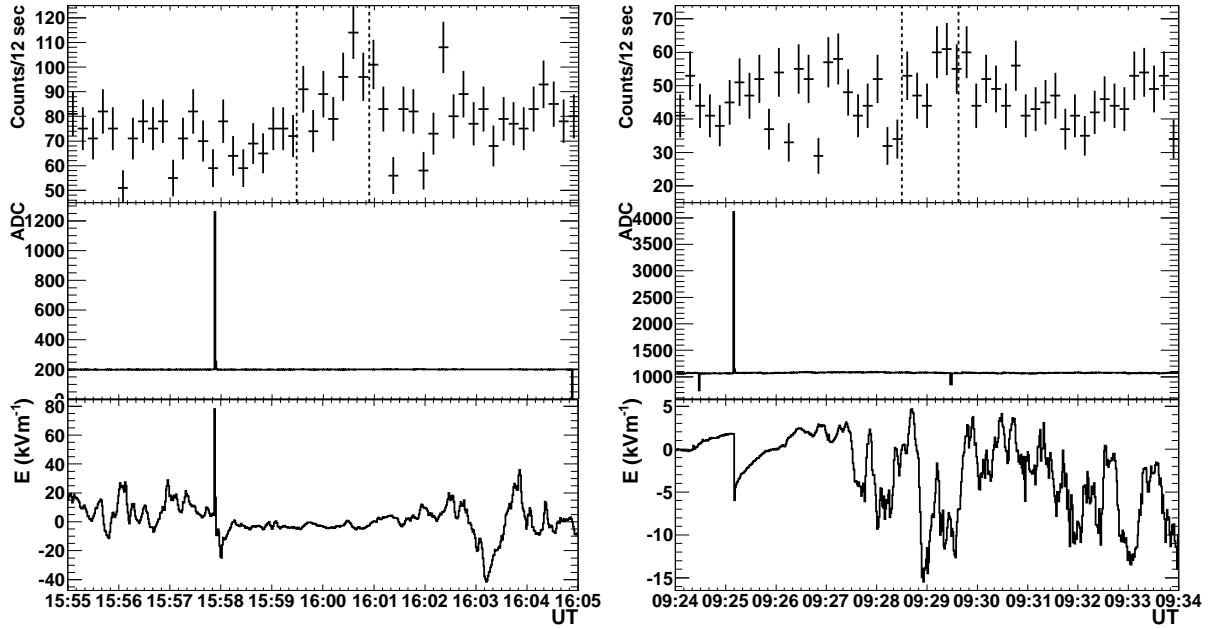
**Figure 6.** The count-rate histories of the plastic scintillator of Detector A and the environmental sensors. Left panels show 071213, obtained over 15:55 − 16:05 UT, while right ones represent 081225, obtained for 9:24 − 9:34 UT. Top, middle and bottom panels in both sides represent a > 1 MeV counts every 12 sec from the plastic scintillator, 1-sec optical data variations, and 1-sec electric field ones, respectively. All abscissa are universal time. Vertical lines in top panels represent the burst periods.
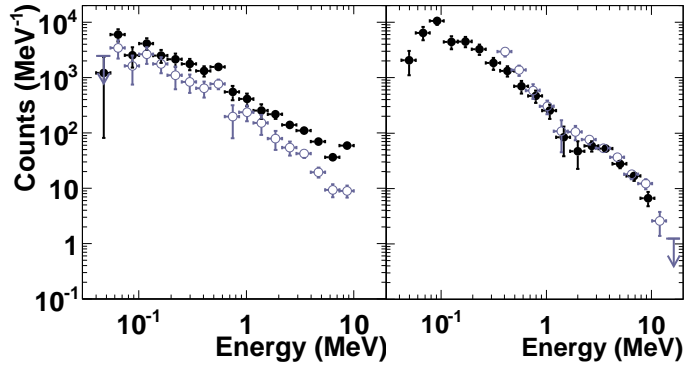
**Figure 7.** Background-subtracted spectra of Detector-A (left) and B (right) of 071213. Black and gray points in the left panel indicate the NaI data without and with anticoincidence, respectively, while those in the right panel show the NaI and CsI scintillators, respectively. All error bars quoted are statistical $1\sigma$. Arrows, showing 95% confidence level upper limits, are drawing when statistical significance of a data point is lower than $1\sigma$. The horizontal and vertical axes show the photon energy in MeV and count per unit energy interval, respectively. Detector responses have not been removed.
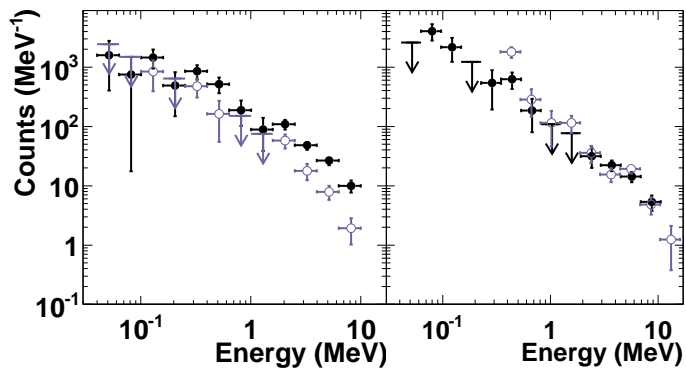


**Figure 8.** The same as Fig. 7, but for the 081225 event.
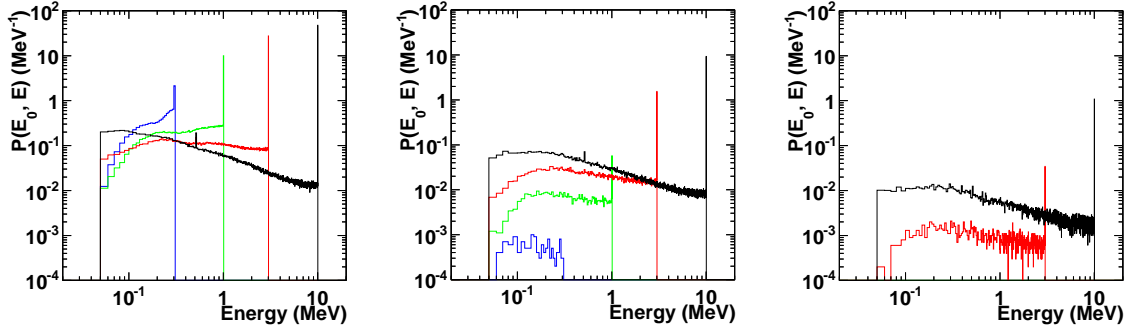
**Figure 9.** Photon spectra at the observatory derived from Monte Carlo simulations. Three panels correspond to $d = 300$ m (left), 1000 m (middle), and 2000 m (right). Different colors denote incident photon energies, $E_0 = 0.3$ (blue), 1 (green), 3 (red), and 10 MeV (black) in all panels. Abscissa shows the photon energy at the observatory, while ordinate represents probability density function.
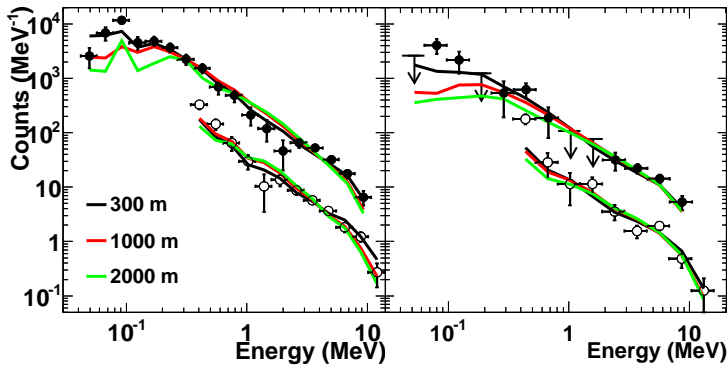


**Figure 10.** The photon spectra observed by the NaI (filled circles) and CsI (open circles) scintillators of Detector-B, compared with calculations for assumed source distances of 300 m (black), 1000 m (red), and 2000 m (green). Left panel shows 071213, while right one indicates 081225. For clarity, the CsI data and the corresponding model spectra are multiplied by 0.1. The horizontal and vertical axes show the photon energy in MeV and counts in each bin, respectively.
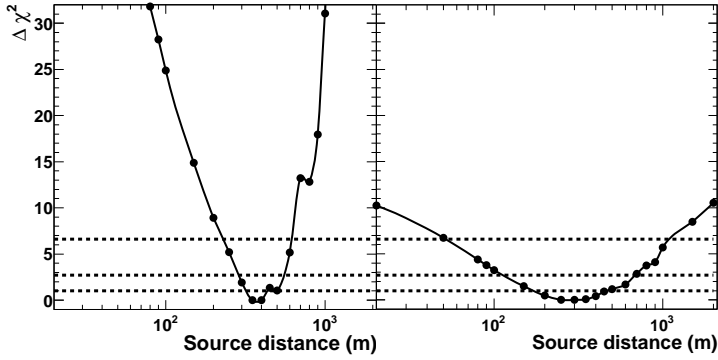
**Figure 11.** The values of $\Delta\chi^2 = \chi^2 - \chi^2_{\min}$, plotted as a function of the assumed source distances (black circles). Left and right panels show 071213 and 081225, respectively. Black curves show smoothing lines. Horizontal dashed lines from bottom to top correspond to 68%, 90%, and 99% confidence level.
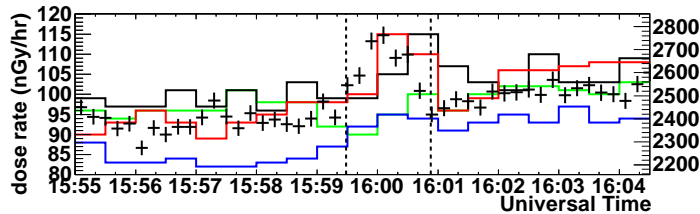


**Figure 12.** Radiation dose rates per 30 sec (left ordinate) obtained by ion chambers of radiation monitors over $15{:}55 - 16{:}05$ UT on 2007 December 13. Different colors specify the radiation monitors numbered as 4 (green), 5 (black), 6 (red), and 7 (blue) in Fig. 1. Superposed on them, crosses show the $> 40$ keV count history per 12 sec of the NaI detector of Detector-B (right ordinate). Vertical dashed lines represent the defined start and end time of the 071213 event.
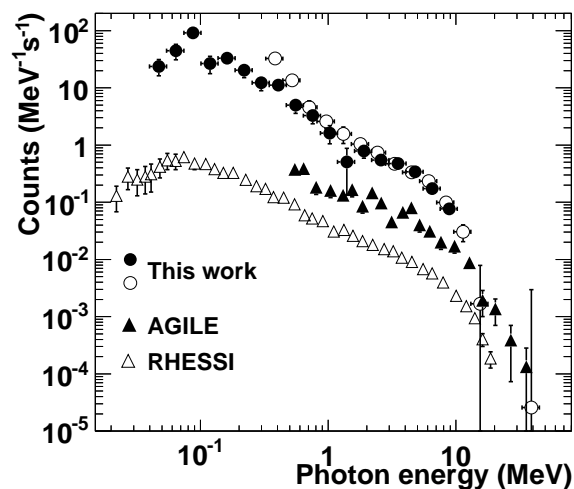
**Figure 13.** Cumulative spectra of the three GROWTH events from Detector-B [NaI and CsI (filled and open circles, respectively)], compared with summed TGF spectra by RHESSI and AGILE. The latter two spectra are adopted from Fig.2 of *Dwyer and Smith* [2005] and Fig.5 of *Marisaldi et al.* [2010a]. For clarity, the RHESSI and AGILE spectra are multiplied by $1 \times 10^{-5}$ and $1 \times 10^{-4}$, respectively. The vertical and horizontal axes represent counts in $\mathrm{MeV^{-1}s^{-1}}$ and photon energy in MeV, respectively. Errors assigned to the GROWTH and AGILE data are statistical ones, while those for RHESSI include systematic uncertainty of background estimation [*Dwyer and Smith*, 2005].

**Table 1.** The count enhancements and the corresponding photon number flux of 071213 and 081225.

| | 071213 | | | 081225 | | |
|---|---|---|---|---|---|---|
| $\Delta E$ (MeV) | Det. A[a] | Det. B[b] | flux[c]$(\times 10^{-2}\text{cm}^{-2}\text{s}^{-1})$ | Det.A[a] | Det. B[b] | flux[c]$(\times 10^{-2}\text{cm}^{-2}\text{s}^{-1})$ |
| $0.04 - 0.3$ | $530 \pm 70$ | $1120 \pm 110$ | $20.2 \pm 1.9$ | $300 \pm 60$ | $390 \pm 90$ | $6.1 \pm 1.7$ |
| $0.3 - 3$ | $900 \pm 80$ | $1660 \pm 140$ | $22.2 \pm 2.3$ | $400 \pm 60$ | $920 \pm 110$ | $7.6 \pm 2.1$ |
| $3 - 10$ | $410 \pm 30$ | $370 \pm 20$ | $10.5 \pm 1.0$ | $180 \pm 20$ | $178 \pm 16$ | $6.8 \pm 0.9$ |

[a] Sum of the two NaI detectors.

[b] The $0.04 - 0.3$ MeV count correspond to the NaI detector, while the others a sum of the NaI and CsI detectors.

[c] The flux is calculated by the data of Detector-B.

**Table 2.** The obtained spectral parameters and $\chi^2$/d.o.f. of the 071213.

| | P. L. [a] | Exp. P.L. [b] | Exp. P.L. (fix) [c] |
|---|---|---|---|
| $\alpha$ (MeV$^{-1}$sr$^{-1}$) | $(1.25 \pm 0.03) \times 10^{11}$ | $(7.19 \pm 0.02) \times 10^{10}$ | $(4.9 \pm 0.6) \times 10^{9}$ |
| $\beta$ | $2.03 \pm 0.02$ | $1.88 \pm 0.01$ | $1.2 \pm 0.1$ |
| $\epsilon_\text{c}$ (MeV) | $-$ | $50 \pm 20$ | $7$ |
| $\chi^2_{\min}$/d.o.f.[d] | $46.5/28$ $(1.6\%)$ | $46.0/27$ $(1.3\%)$ | $49.6/28$ $(0.72\%)$ |
| $d$ (m) [e] | $400^{+160}_{-110}$ | $350^{+210}_{-240}$ | $150^{+60}_{-70}$ |

[a] Power law model.

[b] Exponentially cut-off power law model.

[c] Exponentially cut-off power law with $\epsilon_\text{c}$ being fixed at 7 MeV.

[d] Values in parentheses represent the probability with the given $\chi^2_{\min}$ and d.o.f..

[e] Quoted errors of $d$ are 90% confidence values, while other errors are 68% ones.

**Table 3.** The obtained spectral parameters and $\chi^2$/d.o.f. of 081225.

| | P. L. | Exp. P.L. | Exp. P.L. (fix) |
|---|---|---|---|
| $\alpha$ (MeV$^{-1}$sr$^{-1}$) | $(1.21 \pm 0.09) \times 10^{9}$ | $(6.4 \pm 1.0) \times 10^{9}$ | $(5.1 \pm 0.4) \times 10^{8}$ |
| $\beta$ | $1.61 \pm 0.03$ | $1.48 \pm 0.09$ | $0.87 \pm 0.02$ |
| $\epsilon_\text{c}$ (MeV) | $-$ | $70 \pm 80$ | $7$ |
| $\chi^2_{\min}$/d.o.f. | $40.9/20$ $(0.38\%)$ | $40.6/19$ $(0.25\%)$ | $43.8/20$ $(0.16\%)$ |
| $d$ (m) | $300^{+390}_{-180}$ | $250^{+430}_{-210}$ | $100^{+280}$ [a] |

[a] The lower value were unable to be determined.

**Table 4.** The $N_\text{e}$ estimated for 071213 and 081225.

| | 071213 | | 081225 | |
|---|---|---|---|---|
| $\theta_{\max}$(deg.) | $H = 300$ m | $H = 1000$ m | $H = 300$ m | $H = 1000$ m |
| 15 | $1.9 \times 10^{10}$ | $6.2 \times 10^{9}$ | $3.7 \times 10^{9}$ | $1.2 \times 10^{9}$ |
| 30 | $4.7 \times 10^{11}$ | $1.5 \times 10^{11}$ | $9.3 \times 10^{10}$ | $3.0 \times 10^{10}$ |